nature materials

SUPPLEMENTARY INFORMATION

https://doi.org/10.1038/s41563-019-0478-1

In the format provided by the authors and unedited.

Titanium-carbide MXenes for work function and interface engineering in perovskite solar cells

A. Agresti[1,2,7], A. Pazniak[3,7], S. Pescetelli[1,7], A. Di Vito[1], D. Rossi[1], A. Pecchia[4], M. Auf der Maur[1], A. Liedl[5], R. Larciprete[5,6], Denis V. Kuznetsov[3], D. Saranin[2] and A. Di Carlo[1,2]*

[1]Centre for Hybrid and Organic Solar Energy, Department of Electronic Engineering, University of Rome Tor Vergata, Rome, Italy. [2]Laboratory of Advanced Solar Energy, National University of Science and Technology 'MISiS', Moscow, Russia. [3]Department of Functional Nanosystems and High-Temperature Materials, National University of Science and Technology 'MISiS', Moscow, Russia. [4]Istituto per lo Studio Materiali Nanostrutturati—CNR, Rome, Italy. [5]INFN-LNF, Frascati, Italy. [6]CNR-Institute for Complex Systems, Rome, Italy. [7]The authors contributed equally: A. Agresti, A. Pazniak, S. Pescetelli.
*e-mail: aldo.dicarlo@uniroma2.it

A) Material characterization

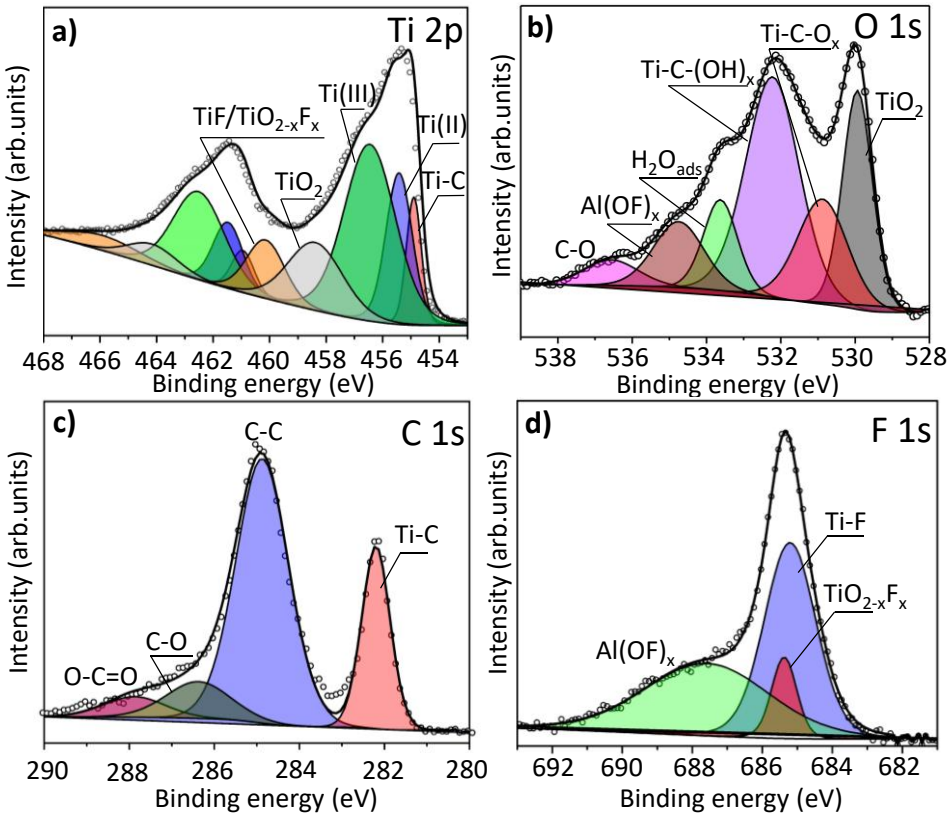

Figure S1: High-Resolution a) Ti 2p, b) O 1s, c) C 1s, d) F 1s X-Ray photoelectron spectra (XPS) of $Ti_3C_2T_x$ MXene; open circles represent experimental data while the continuous bold black line is the final fit obtained by summing the Gaussian-Lorentzian fits related to each component (the different colours peaks under the spectra represent various moieties).

Gaussian-Lorentzian fitting of the XPS Ti 2p spectrum in MXene (**Figure S1a**) reveals that titanium appears in five doublets (Ti $2p_{3/2}$ – Ti $2p_{1/2}$). The main Ti 2p components are fitted as Ti-C, Ti(II), Ti(III) that could be attributed to Ti atoms bonded to C at a Binding Energy (BE) = 455.0 (461.3) eV and Ti(II) and Ti(III) atoms bonded with –O or –OH at BE= 455.8 (461.4) eV and 457.0 (462.8) eV, respectively.[1] In this case, Ti-C, Ti(II), Ti(III) species form the majority fraction (~82 %) of the Ti2p spectrum. The minor Ti $2p_{3/2}$ components centered at 458.4 eV and at 459.5 eV belong to TiO_2 and $TiO_{2-x}F_x$ or Ti-F species, respectively. The O1s region in the XPS spectrum of the MXene (**Figure S1b**) is fitted by components corresponding to C-Ti-$(OH)_x$ at BE = 532.1 eV, C-Ti-O_x at BE = 531.2 eV, and TiO_2 at BE = 529.9 eV. Additionally, small fractions of H_2O_{ads}, $Al(OF)_x$, and C-O are present. Carbon appears in four bonds (**Figure S1c**); the peak at BE of 282.2 eV corresponds to the carbide component Ti-C in MXene, while the other three peaks are attributed to graphitic C-C or CH_x, originated from selective dissolution of Ti during chemical etching, and to surface contaminations of C-O and COO observed at 286.3 eV and 288.1 eV, respectively. The major component in the F 1s region (**Figure S1d**) is C-Ti-F_x at a BE of 685.0 eV. The sample contains fractions of $TiO_{2-x}F_x$ and $Al(OF)_x$ at a BE of 685.3 eV and 688.3 eV, respectively. To get exact information about functional groups and their ratio we used the survey spectrum of $Ti_3C_2T_x$ (**Figure S2a**) and the high-resolution O 1s and F 1s spectra (**Figures S1b, S1c**). The ratio between the F : OH : O functional groups is equal to 1.6 : 0.65 : 0.34. Based on these results, it can be concluded that the MXene surface randomly ends with the F, OH and O groups, with a prevalence of fluorine functional groups.

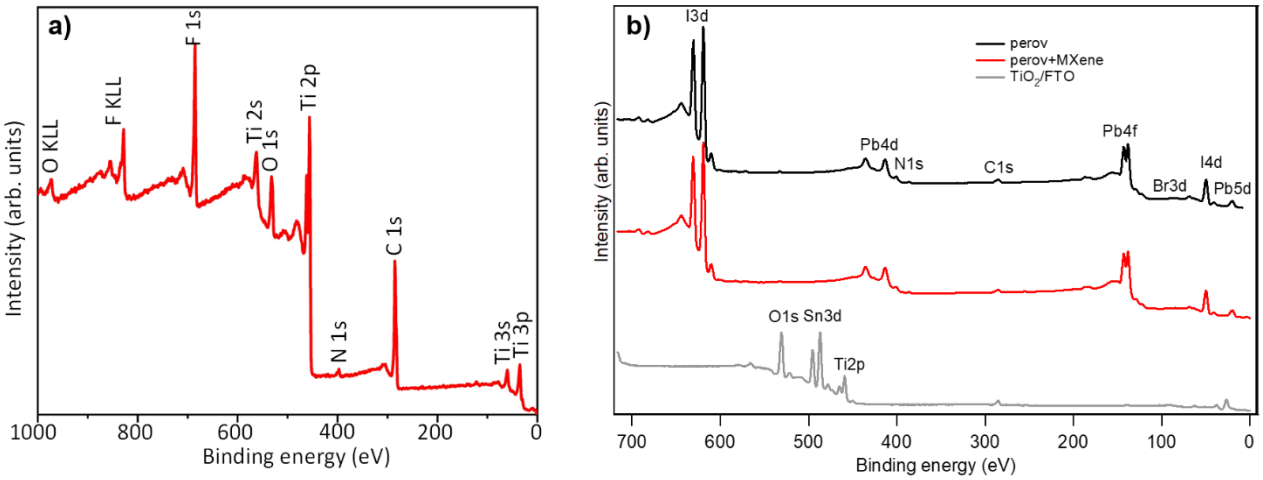

Figure S2: a) The survey spectrum of the $Ti_3C_2T_x$ MXene. The tiny N1s peak can be due to minimal residual of the ACN solvent used during the MXene preparation procedure. b) XPS spectra measured at photon energy of 1253.6 eV on undoped and doped perovskite films. The bottom curve shows, for comparison, the XPS spectrum of the TiO_2/FTO substrate. The complete lack in both spectra of any intensity in correspondence of the substrate peaks indicates that the perovskite layers are complete and that, due to their thickness (150 nm), substrate photoelectrons do not emerge from the sample surfaces and do not contribute to the photoemission spectra. Due to the low concentration of Mxene, the characteristic $Ti_3C_2T_x$ spectral features shown in Figure S1 are not detected in the spectrum of the MXene-doped perovskite.

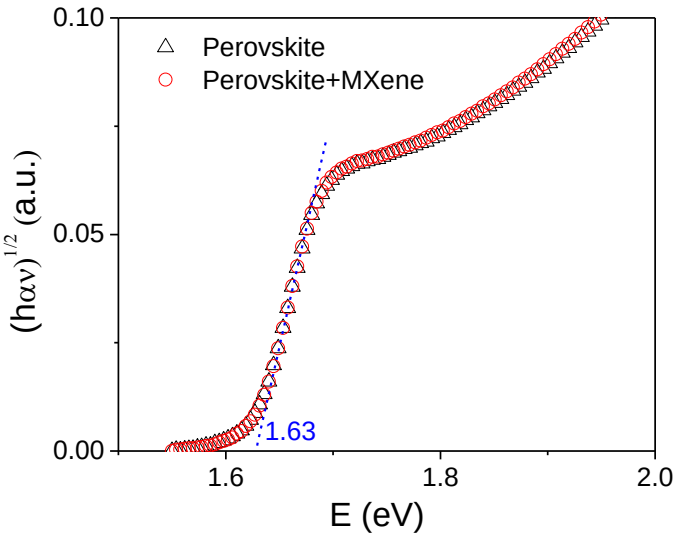

Figure S3: Tauc plot of multi-cation perovskite with and without MXene doping. In both cases the band gap is estimated around 1.63 eV.

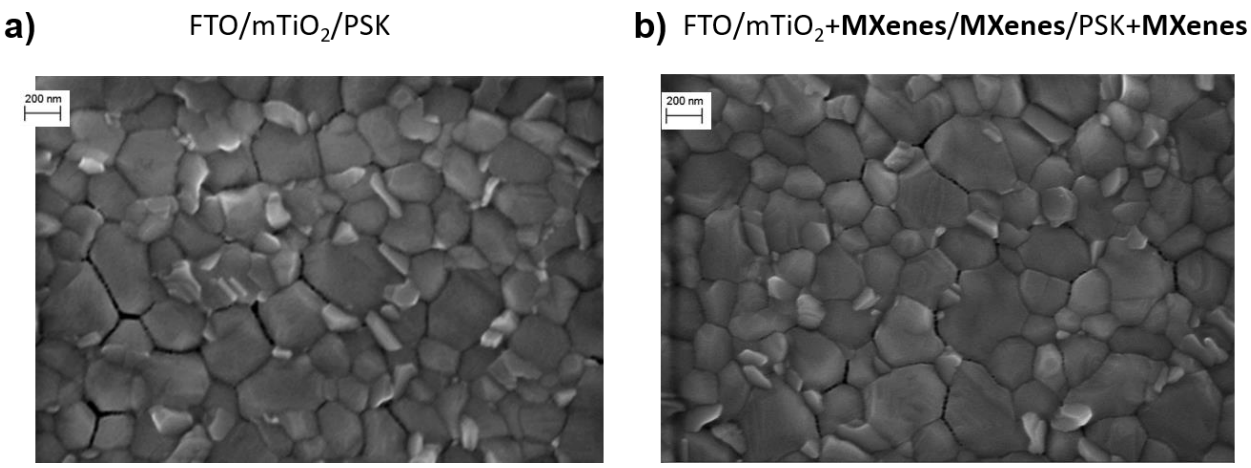

Figure S4: Scanning Electron Microscopy (SEM) images acquired on opened perovskite (PSK) photo-electrode (PE) for reference (ref) and Type C devices.

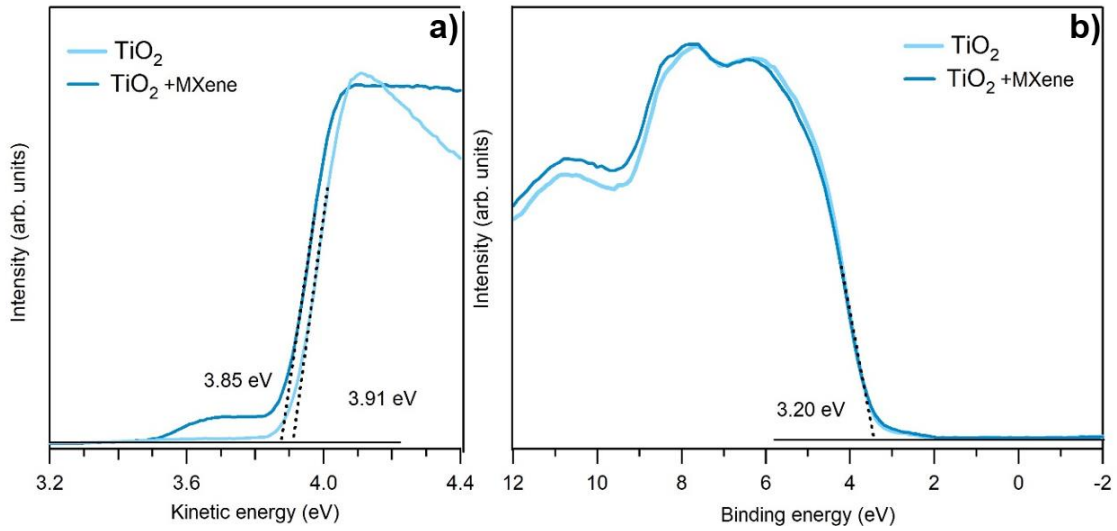

Figure S5: UPS spectra measured with photon energy of 40.8 eV on the TiO_2 electrode with and without the addition of MXene; a) left panel and b) right panel showing secondary electron cut-off and valence band region, respectively.

When annealing the $Ti_3C_2T_x$ MXene in air at high temperature an oxidation to TiO_2 is observed as reveled by XPS data reported in Figure S6. We can assume that also the MXene dispersed in the TiO_2 matrix undergoes a similar oxidative process when annealed in air.

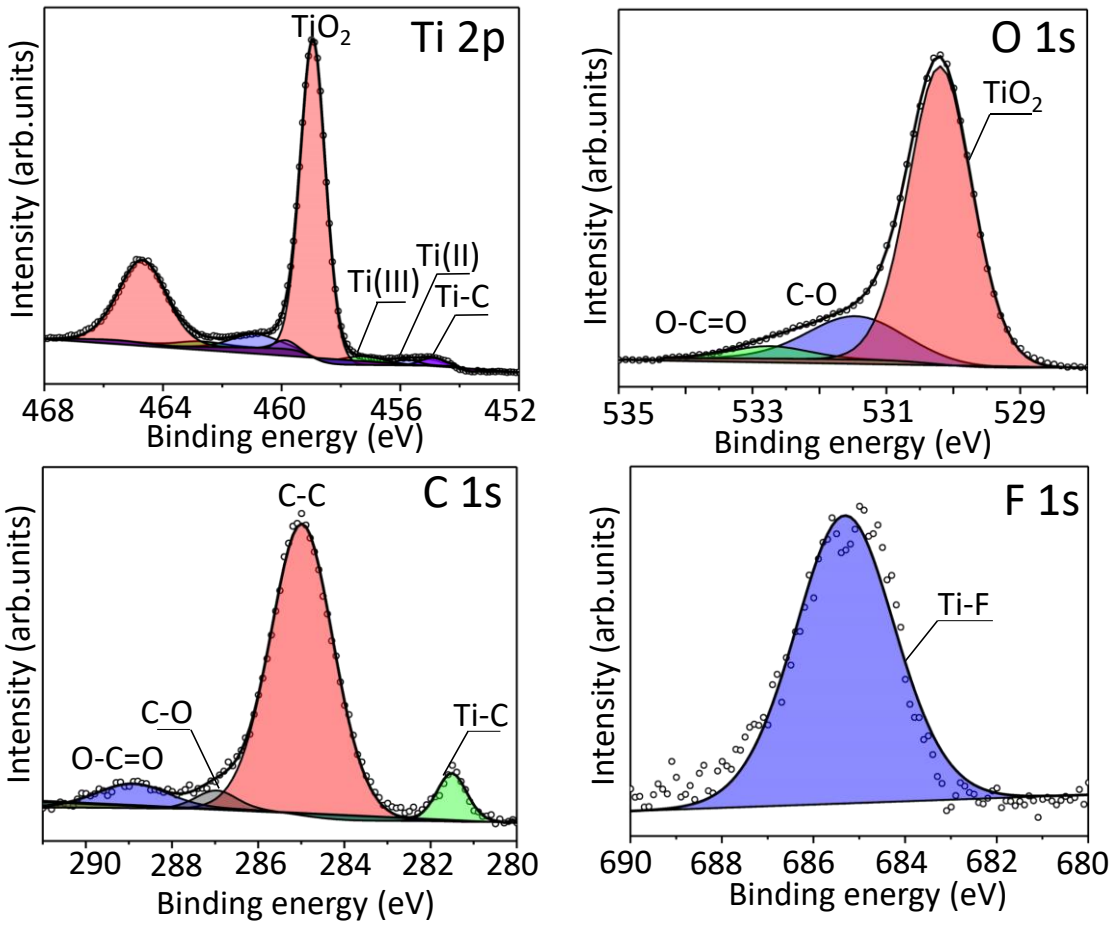

Figure S6: High-resolution Ti 2p, O 1s, C 1s, and F 1s core level XPS spectra taken on a $Ti_3C_2T_x$ sample annealed to 400 °C in air.

According to XPS measurements (Figure S6) the surface chemistry of MXene after annealing changes. The Ti 2p3/2 peaks at 454.9, 455.7, and 457.2 eV almost disappears, accompanied with a decrease in the intensity of Ti–C bond and an increase of TiO_2 for the Ti 2p spectrum, as compared with fresh $Ti_3C_2T_x$ MXene. Correspondingly, for the spectrum of C 1s (Figure S6), the intensity of C–Ti centered at 281.5 eV decreases substantially, demonstrating that TiO_2 nanoparticles and free carbon are formed at the expense of $Ti_3C_2T_x$ MXene. We can assume that also the MXene dispersed in the TiO_2 matrix undergoes a similar oxidative process when annealed in air.

XRD spectrum for $mTiO_2$ layer doped with MXene presents a small peak for 7.5° typical of MXenes which is not present in the XRD of sintered pristine $mTiO_2$. (Figure S7). This is in agreement with the XPS data of Figure S6 showing that the oxidation process is not complete.

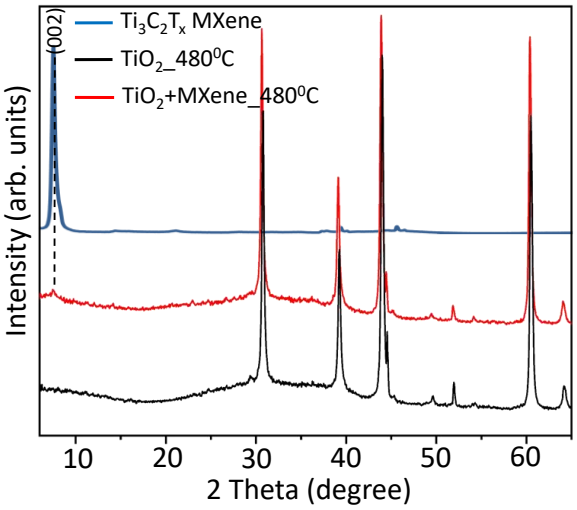

Figure S7: XRD spectra of fresh powder of MXene and of undoped and MXene-doped TiO_2 deposited on FTO and annealed at 480 °C, which shows the (002) reflection typical of the crystalline Ti_3C_2 phase.

Differently, we can confidently assume the thermal stability of MXenes when used for perovskite layer doping and for TiO_2/MXene/Perovskite interlayer. In both cases, MXene is processed after the sintering of TiO_2 with temperature that never exceed 100 °C. In fact, Persson et al.[2] showed that Ti_3C_2Tx samples are stable up to 500 °C and that F desorption is occurred in the 550-700 °C interval, and Hart et al.[3] identified the OH release with the m/e=17 peak observed at 375 °C in the ion current.

We verified that WF shift induced by the MXene is also present in other halide perovskites. To this end, we performed UPS characterization on the $CH_3NH_3PbI_3$ ($MAPbI_3$) perovskite with and without MXene doping. Here, we used the same doping strategies for the multi-cation perovskite described in the experimental section. UPS results are shown in **Figure S8**

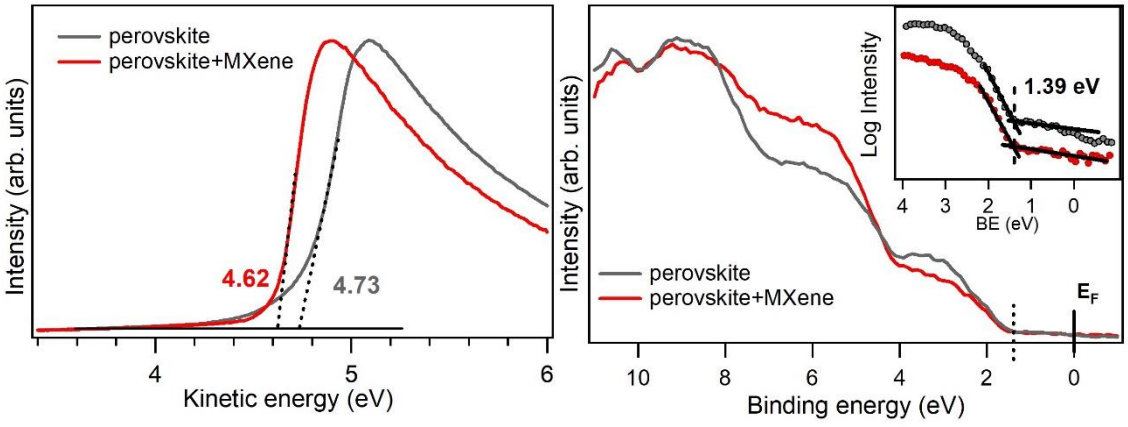

Figure S8: UPS spectra measured with photon energy of 40.8 eV on $MAPbI_3$ perovskite with and without the addition of MXene; left panel and right panel showing secondary electron cut-off and valence band region, respectively. The inset in left panel shows the photoemitted intensity plotted in logarithmic scale for the VBM determination at the intercept with the baseline. The curves are vertically shifted for clarity.

A WF shift of 0.11 eV has been measured between pristine $MAPbI_3$ and MXene-doped $MAPbI_3$. As in the case of the multi-cation perovskite, after the addition of MXene no appreciable difference in valence band maximum is observed which lies 1.39 eV below the Fermi level.

B) DFT calculations

First-principles calculations based on density functional theory (DFT) within the local density approximation (LDA) are performed using the Quantum Espresso package.[4] Scalar-relativistic norm-conserving pseudopotentials are employed, with the exchange-correlation energy parameterized by Perdew-Zunger.[5] To the perovskite/MXene interaction, we considered a $CH_3NH_3PbI_3$ ($MAPbI_3$) perovskite structure in its high temperature cubic phase and a $Ti_3C_2T_x$ MXene layer, with the T_x terminal group being O or OH. The simulations are performed using a slab configuration with approximately 25 Å of $MAPbI_3$ and more than 15 Å of vacuum. On top of the MAI_2 terminated $MAPbI_3$ layer, 2×2 units of $Ti_3C_2T_x$ are placed in the x-y plane, the z direction being perpendicular to the perovskite/MXene interface. We fix the lattice constants of MXene to their optimized values and adapt the lattice constants of $MAPbI_3$ accordingly. The schematic representation of the structure in the x-y plane parallel to the interface is shown in the left panel of **Figure S9**. To study the TiO_2/MXene interface, we considered a slab comprising approximately 20 Å of TiO_2 anatase and more than 20 Å of vacuum. On top of the (101) surface of TiO_2, 1×4 units of $Ti_3C_2T_x$ are placed in the x-y plane, with the z direction orthogonal to the interface. Due to the pronounced mismatch between the crystal structures of the considered materials, the lattice constants of TiO_2 strongly deviate from the equilibrium values, in order to match the periodicity of $Ti_3C_2T_x$ (see **Figure S9**, right panel). For all the considered settings, the slab structure is relaxed until the residual force on each atom is below 10^{-2} eV/Å, a 4×4×1 Monkhorst-Pack grid is used for reciprocal space integration and the electronic wave functions are expanded onto a plane-wave basis set with an energy cut-off of 70 Ry and 50 Ry for the $MAPbI_3$/MXene and the TiO_2/MXene systems, respectively.

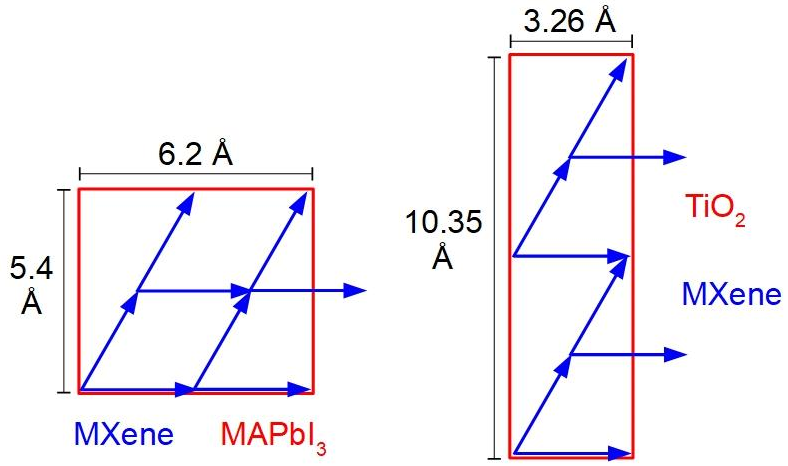

Figure S9: Schematic representation of the simulated slab structure in the x-y plane parallel to the $MAPbI_3$/MXene (left panel) and TiO_2/MXene (right panel) interface.

In **Figure S10a**, the work function of bare and functionalized Ti_3C_2 with O, F and OH terminal groups is reported. In this case, we applied also the generalized gradient approximation (GGA) of Perdew-Burke-Ernzerhof (PBE) for the exchange-correlation functional,[6] in order to test the accuracy of LDA calculations and compare our results with the reference DFT-GGA study of Khazaei et al.[7] The ionization potential of cubic $MAPbI_3$ and $FAPbI_3$ and of TiO_2 anatase (101) is depicted in **Figure S10b**. Here, we reported also the value obtained for the PbI_2 terminated surface of $MAPbI_3$, to be compared with the DFT-PBE analysis of Foley et al.[8] We can say that LDA results are reasonably accurate with respect to GGA calculations and previous theoretical works.[9]

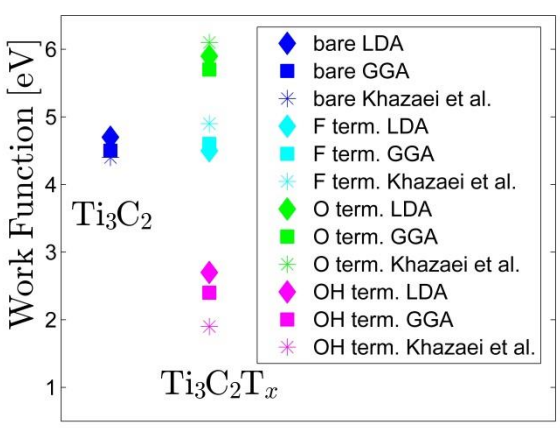

a)

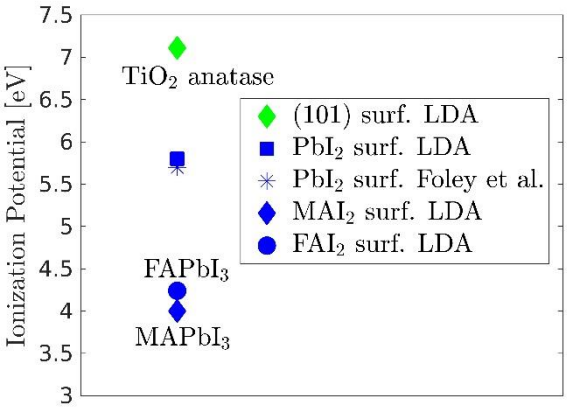

b)

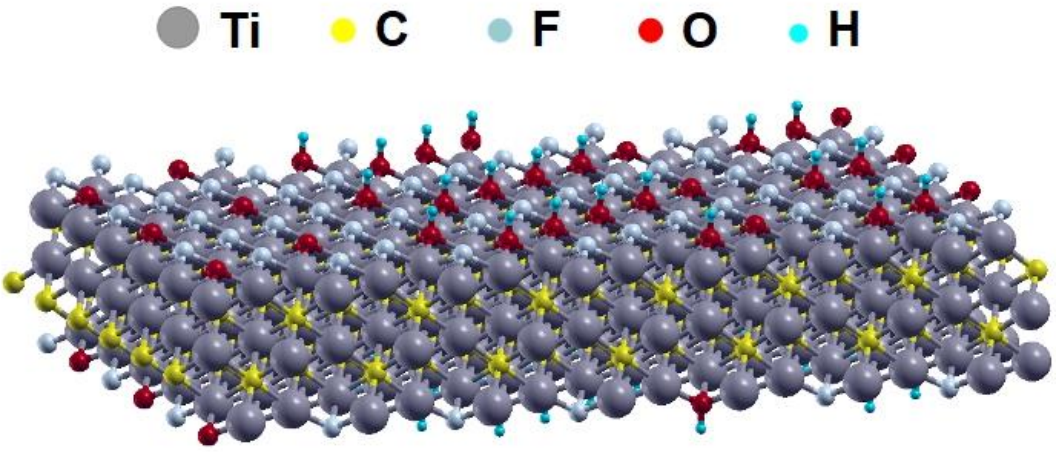

c)

Figure S10: a) Work function of bare and functionalized Ti_3C_2 with O, F and OH terminal groups. The comparison between LDA and GGA calculations and the results of Khazaei et al. is shown. b) Ionization potential of TiO_2 anatase (101) and MA(FA)PbI_3 in its high temperature cubic phase. The results for the PbI_2 and the MAI_2 surface of $MAPbI_3$ are shown. The former is compared with the study of Foley et al. c) Structure of the MXene slab with mixed F, OH and O functional groups randomly distributed with relative amount 62:25:13 in agreement with XPS measurements (Figure S1, S2a).

Concerning the mixed termination case, a WF value in the range of 4.0-4.27 eV can been calculated considering a linear interpolation of the WFs for MXene with the different terminations (**Figure S10a**) and for the experimental F:OH:O ratio measured with XPS (**Figure S1,S2a**). This value compares reasonably well with the experimental results of 3.69 eV (**Figure 1c**). The discrepancy is mainly related to the non-linear behaviour of WF with respect to termination mix.[10] In order to be more quantitative on this point, we calculate the MXene WF with F, OH and O functional groups randomly distributed on MXene surface with a relative amount of 62:25:13 in agreement with XPS measurements (**Figure S1,S2a**). The simulations are performed using a slab configuration, reported in **Figure S10c**, with approximately 1 nm of MXene and 3.3 nm of vacuum. The slab contains 28 MXene unit cells. We assume completely functionalized MXene surfaces and the symmetry between top and bottom surfaces is preserved. The DFT-LDA calculation provide a WF= 3.75 eV in very good agreement with the experimental result. These results underline the non-linear contribution of the terminal group to the MXene WF.

In **Figure S11**, a symmetric stack $Ti_3C_2(OH)_2/MAPbI_3/Ti_3C_2(OH)_2$ is considered. There is a considerable reduction of work function at both interfaces, as expected from the $MAPbI_3/Ti_3C_2(OH)_2$ slab simulations presented in the main text.

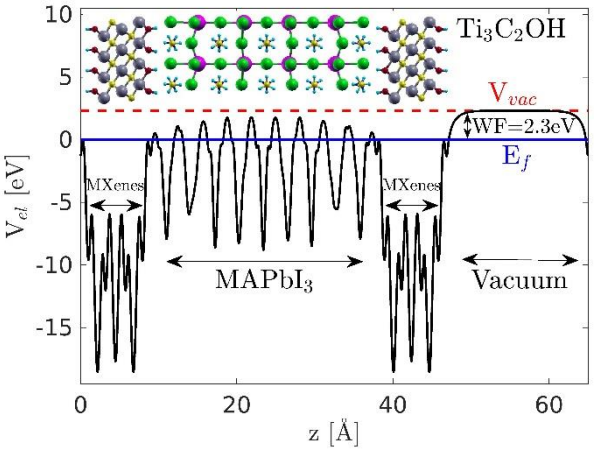

Figure S11: Plane averaged electrostatic potential plotted along the direction perpendicular to the $Ti_3C_2(OH)_2/MAPbI3/Ti_3C_2(OH)_2$ interface. The zero in the ordinate corresponds to the Fermi energy. The work function of the system is shown. The slab structure used to perform the simulations is depicted within the plot, where green, magenta, blue, yellow, cyan, grey and red spheres represent I, Pb, N, C, H, Ti and O atoms, respectively.

In **Figure S12a** the x-y plane averaged electrostatic potential is plotted along the z direction perpendicular to the $FAPbI_3/Ti_3C_2(OH)_2$ interface, where the Fermi energy is set to zero. The projected band structure of this system is shown in **Figure S12b**, where the entity of the contribution from $FAPbI_3$ orbitals is represented with different colours. We can see that the behavior of $FAPbI_3$ at the interface with $Ti_3C_2(OH)_2$ is qualitatively similar to $MAPbI_3$, in terms of charge transfer and work function tuning, albeit the WF of $FAPbI_3$+Ti_3C_2OH is even smaller (1.6 eV compared to 2.1 eV).

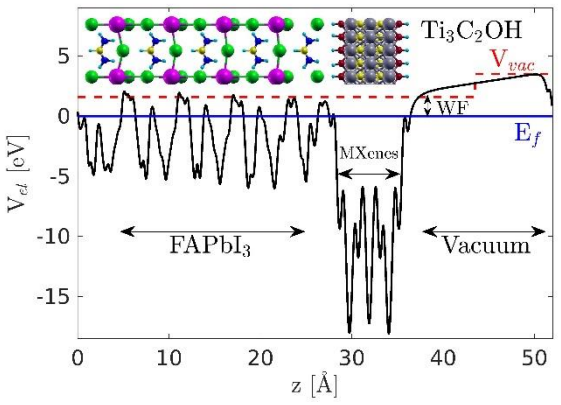

a)

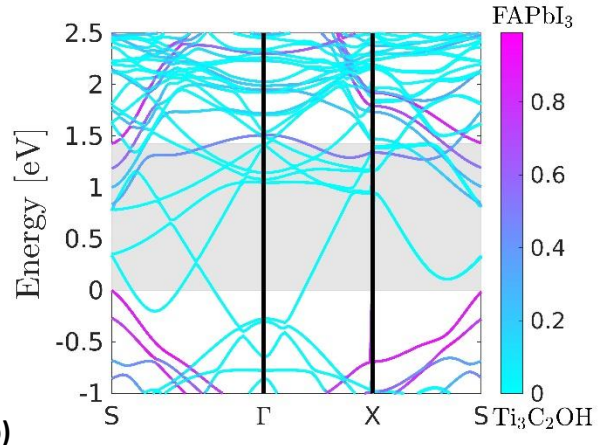

b)

Figure S12: a) Plane averaged electrostatic potential plotted along the direction perpendicular to the $FAPbI_3/Ti_3C_2(OH)_2$ interface. The zero in the ordinate corresponds to the Fermi energy. The work function of the $FAPbI_3$/MXene interface is shown. The slab structure used to perform the simulations is depicted within the plot, where green, magenta, blue, yellow, cyan, grey and red spheres represent I, Pb, N, C, H, Ti and O atoms, respectively. b) Projected band structure of the $FAPbI_3/Ti_3C_2(OH)_2$ interface. The contribution of $FAPbI_3$ orbitals is represented in magenta. The valence band edge of $FAPbI_3$ is set to zero.

In **Figures S13 a)** and **c)**, the x-y plane averaged electrostatic potential is plotted along the z direction perpendicular to the $TiO_2/Ti_3C_2O_2$ and $TiO_2/Ti_3C_2(OH)_2$ interface, respectively, where the Fermi energy is set to zero. An interface dipole is formed at the $TiO_2/Ti_3C_2(OH)_2$ interface, inducing a bending of the vacuum

potential and a reduction of the work function with respect to the $TiO_2/Ti_3C_2O_2$ interface. For both O and OH terminal groups, the Fermi level is shifted towards the TiO_2 conduction band edge, as shown by the projected band structures in **Figures S13 b)** and **d)**, where the entity of the contribution from TiO_2 orbitals is represented with different colours. Note that the Fermi energy shift is more important in the configuration with the OH terminated MXene surface. The functional groups of MXene play an important role in determining the properties of the system. The work function value and the band alignment are affected by the formation of an interface dipole and/or the shift of the Fermi energy with respect to the TiO_2 band edges. The effect of MXene interlayer at the $mTiO_2$/Perovskite interface is well described by the DFT calculations. In this case the MXene interlayer (device type C) is deposited by spray coating technique at low temperature (80°C) that prevent oxidation of Ti_3C_2Tx as discussed in the main text. On the other hand, the oxidation of MXene during the thermal treatment in $cTiO_2$ and $mTiO_2$ deposition can affect the ideal picture presented in the DFT calculation. The final value of the $c/mTiO_2$ WF could be a complex mixture of the nanotitania formed by the oxidation process[11] and the remaining MXene. As discussed, this could be the reason for the small WF shift observed when MXene is added to $c/mTiO_2$ (**Figure S5a**).

We should point out that it is difficult to reach quantitatively predictive calculations because of several uncertainties on the exact surface termination of perovskite, the strain induced on the $MAPbI_3$ crystal in order to match the $Ti_3C_2T_x$ supercell and the inherent approximations in the DFT approach. However, we expect that the trend seen in the DFT study is qualitatively correct, giving an insight into the basic mechanisms at the origin of the perovskite's WF tuning observed in the measurements.

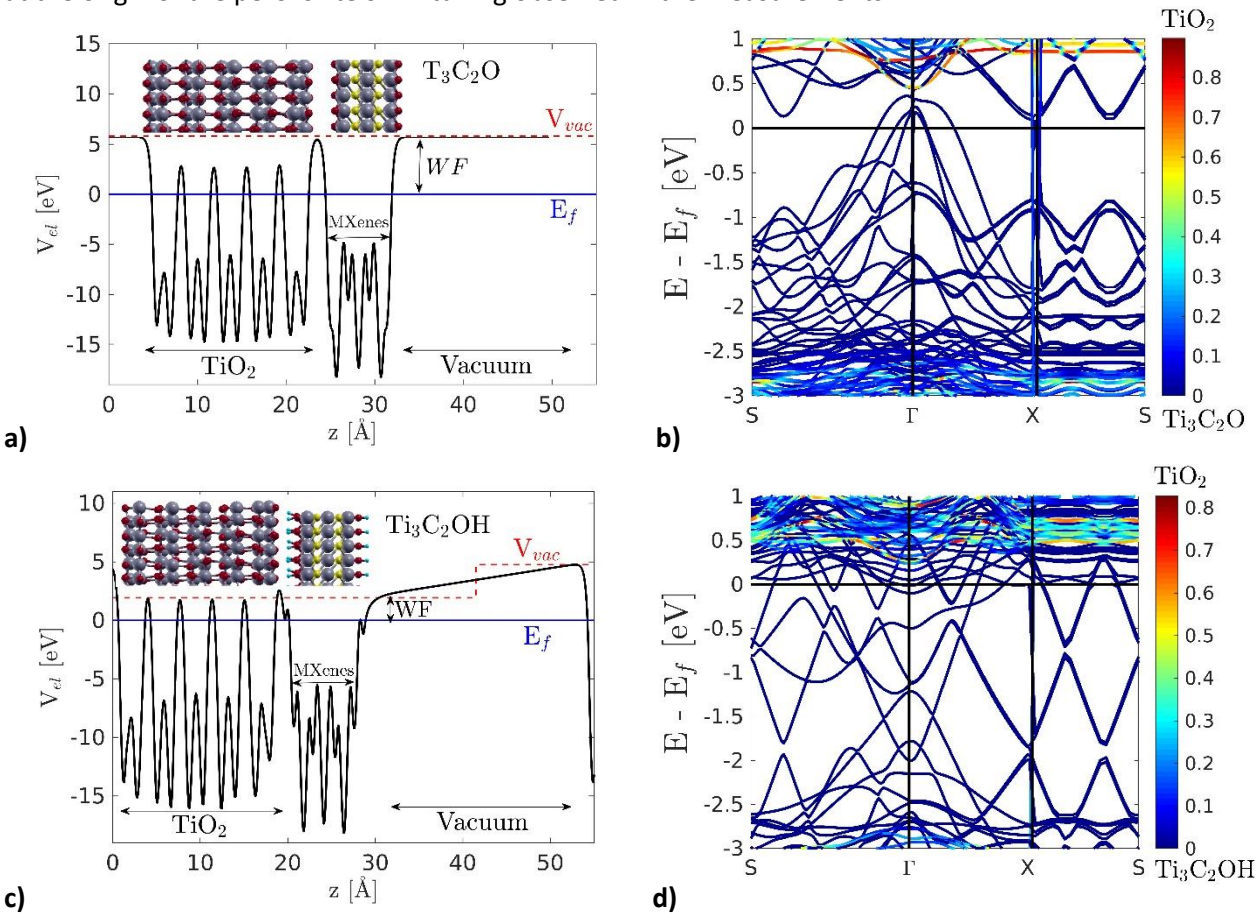

Figure S13: (a) and (c) Plane averaged electrostatic potential plotted along the direction perpendicular to the $TiO_2/Ti_3C_2O_2$ and $TiO_2/Ti_3C_2(OH)_2$ interface, respectively. The zero in the ordinate corresponds to the Fermi energy. The work function of the TiO_2/MXene interface is shown. The slab structure used to perform the simulations is depicted within the plot, where yellow, cyan, grey and red spheres represent C, H, Ti and O atoms, respectively. (b) and (d) Projected band structure of the $TiO_2/Ti_3C_2O_2$ and $TiO_2/Ti_3C_2(OH)_2$ interface, respectively. The contribution of TiO_2 orbitals is represented in red. The Fermi level is set to zero.

C) Device Characterization

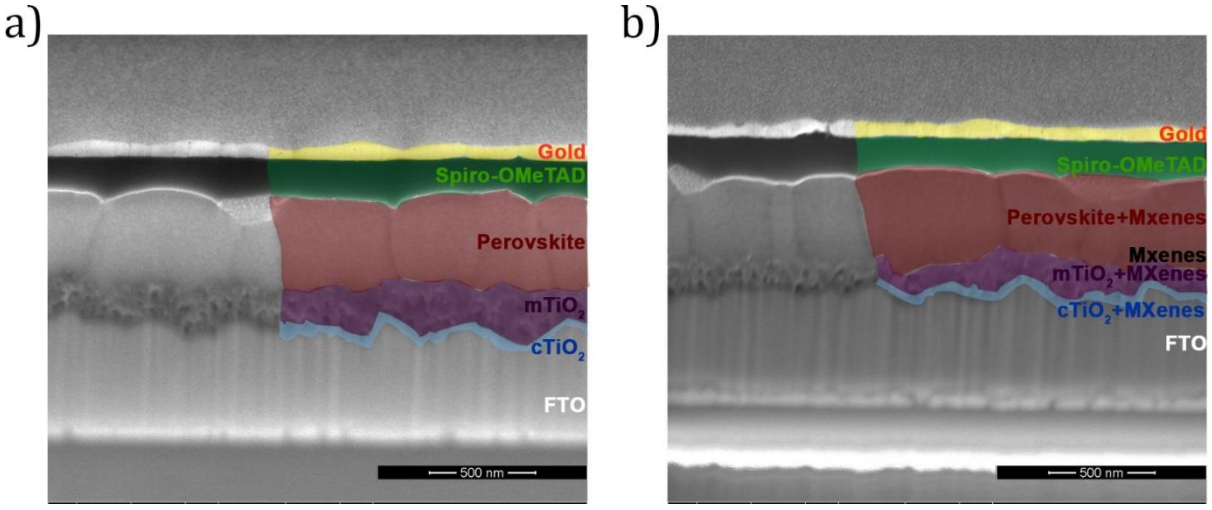

Figure S14: Cross-section SEM images of perovskite solar cells of reference (a) and type C (b) complete devices.

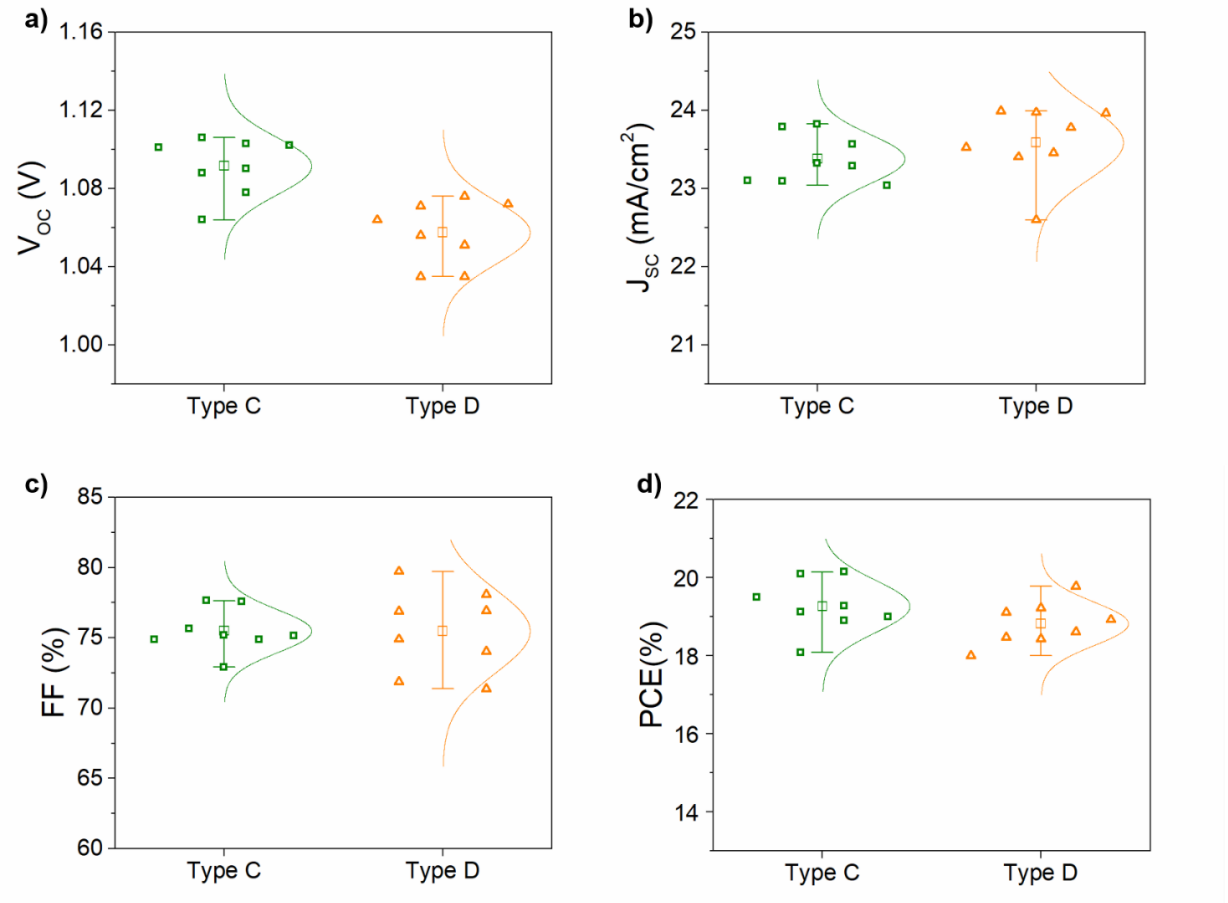

Figure S15: Electrical parameter statistics for the investigated device structures with (type C) and without (type D) addition of MXene within the $cTiO_2$ layer, extracted by the J-V curves acquired at 1 SUN irradiation. The standard error (SE) is represented with a box while the average value is depicted as an empty squared dot. The cell active area is 0.09 cm^2.

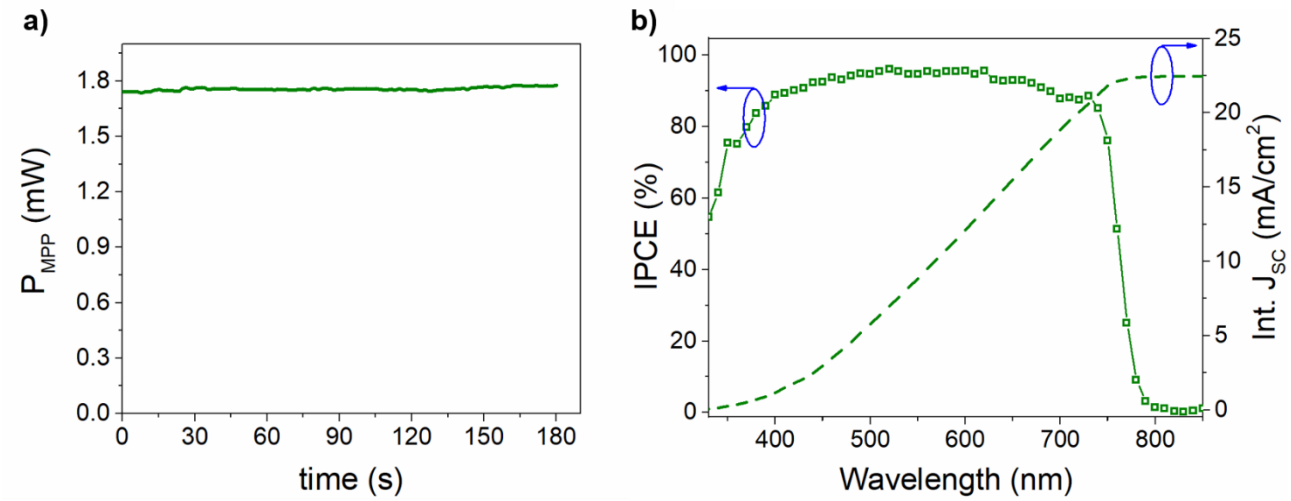

Figure S16: a) Maximum Power Point (MPP) tracking and b) Incident Photon to current Conversion Efficiency (IPCE) spectra with the extrapolated integrated photocurrent density (Integrated J_{SC}) for the best efficient cell type C.

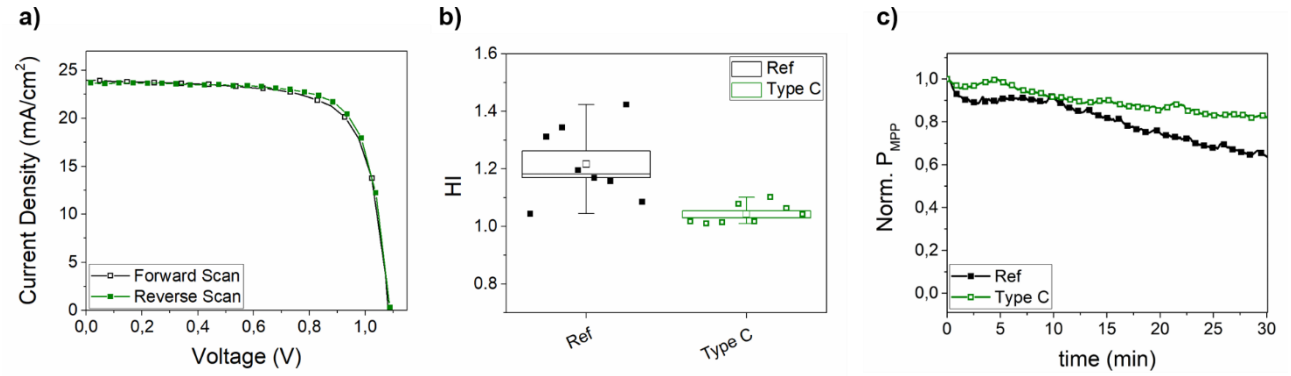

Figure S17: a) Current density-Voltage (J_{SC}-V) curves for forward (black empty squares) and reverse (green full squares) scan for the best efficient device type C. b) Hysteresis Index (HI) statistics for reference and type C devices, in the case of reverse and forward voltage scan during the current-voltage (I-V) characteristic acquisition. c) Power output time-trend for reference and type C devices under prolonged light-soaking at 1 SUN irradiation.

Transient photo-current (TPC) measurements were acquired on reference and type C devices. TPC rise profiles reported in **Figure S18a** show a photocurrent overshoot for reference device that is not present in the case of the MXene-doped cell. According to McNeill et al.[12], the accumulation of trapped charges increases the recombination rate and produces the overshoot. The presence of deep trap states already observed in our recent investigation[13] and ascribed to interstitial iodine defects, can confidently contribute to this current overshoot.[14] Thus, we can conclude that MXene doping reduces the charge trapping efficiency within the device and eventually the hysteresis in the J-V curve. This is further confirmed by the TPC decay profiles reported in **Figure S18b**, where the reference PSC shows a faster exponential current decay after light turn-off with respect to the MXene-doped devices. The charge carrier lifetime reported in **Figure S18c** has been extracted by the V_{OC} fall profiles, acquired at different irradiation levels. The increase of both current decay time and photocarrier lifetimes in MXene-doped devices with respect to reference PSC can be confidently ascribed to a reduction of trap recombination within the perovskite layer or at the $mTiO_2$/perovskite and perovskite/spiro-OMeTAD interfaces.

In order to investigate trap-assisted recombination we measure the V_{OC} as a function of incident light power (P_{inc}) as reported in **Figure S18d**. When the P_{inc} approaches 1 SUN (P_{inc}>0.2 Sun) the generation and recombination rate is dominated by the traps within the perovskite layer or at the TiO_2/perovskite and perovskite/spiro-OMeTAD interfaces, while the TiO_2 trap filling is already completed (**Figure S18d**).[15] Thus, the lower is the V_{OC} (P_{inc}) slope, the lower is the impact of trap states onto the carrier dynamics. Since type A and C structures differ from each other only for the addition of MXene within the ETL, the major difference in the recoded slope can be imputed to a reduction of charge recombination rate at such interface. As a further confirmation, charge carrier lifetimes extracted from TPV decay measurements (**Figure S18c**) show the highest values for the type C structure.

With the aim to clarify the role of MXene interlayer at $mTiO_2$+MXene/perovskite+MXene interface, J_{SC} vs incident power $J_{SC}(P_{inc})$ and photoluminescence (PL) emission were acquired on both type B and C structures. The plots of J_{SC} vs incident power $J_{SC}(P_{inc})$ reported in **Figure S18e** were acquired by progressively varying the white LED power from 0.1 to 1 SUN. The curves can be fitted with a power law, $J_{SC} \propto I^{\alpha}$, where $\alpha = 0.75$ is typical for space charge limited solar cells due to a carrier imbalance or an interfacial barrier, while $\alpha \sim 1$ refers to a device with no space charge effects.[16] Both investigated device structures (type B and C) showed α very close to 1, evidencing no space-charge limited behaviour. However, α is slightly higher in type C PSC with respect to type B, suggesting an improved charge transfer when MXene interlayer is introduced.

Figure S18f reports the photoluminescence (PL) emission spectra acquired on opened PEs for devices type B and C. When the MXene interlayer is introduced, the trap density in the perovskite layer is expected to be the same for both B and C types. On the contrary, the addition of the MXene interlayer at the $mTiO_2$+MXene/perovskite+MXene interface can reduce trap state density or passivate the $mTiO_2$ surface by increasing the PL emission, as showed in **Figure S18f**. This is even shown by the slight blue shift of the PL spectrum recorded in the case of type C PSC compared to type B (see **Figure f**), confirming a passivation of interfacial trap states, as already reported by Shao and co-workers.[17]

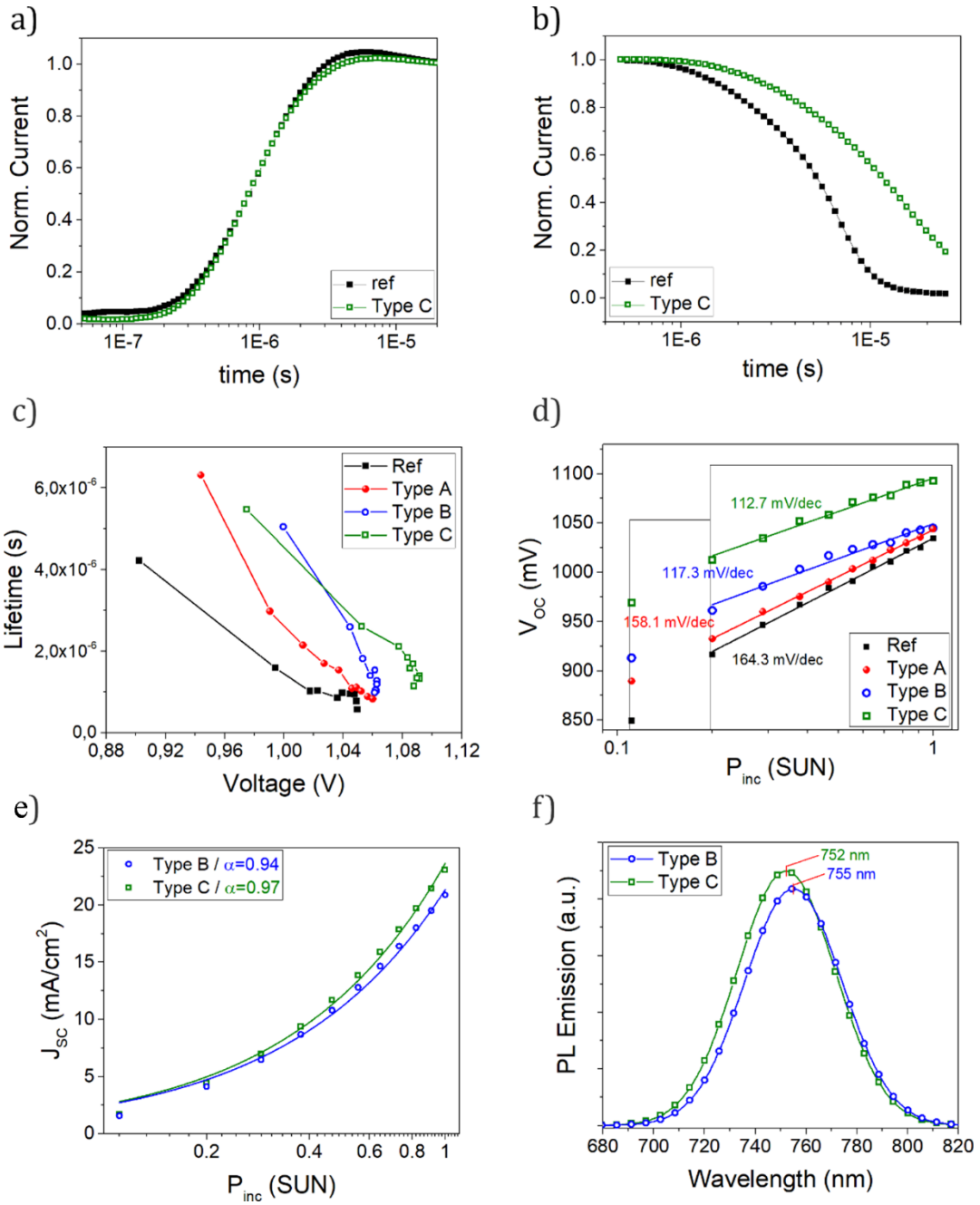

Figure S18: Transient photocurrent rise a) and fall b) profiles acquired on reference (black square dotted curves)-Ref and MXene-based PSCs. c) Charge carrier lifetime extracted by the small-signal transient photovoltage (TPV) decay profiles. In a TPV experiment, the solar cell is kept at open-circuit voltage under bias-illumination. Then an additional small laser pulse (or LED pulse) is applied to the device to create some additional charge that decays exponentially thereafter. Since no current is flowing within the device, the generated charges expire through several recombination channel. The higher is the trapping efficiency of the trap state, the lower is the charge carrier lifetime, as in the case of the reference PSC (black square dots) compared with MXene-doped ones (types A, B and C). d) J_{SC} light intensity-dependence [$J_{SC}(P_{inc})$] for Ref and MXene-based PSC (types A, B and C). The power law $J_{SC} \propto I^{\alpha}$ has been employed to fit the acquired $J_{SC}(P_{inc})$ curves. e) V_{OC} light intensity-dependence [$V_{OC}(P_{inc})$] of PSCs for types B and C; f) Photoluminescence emission (PL) spectra for complete device type B and C without gold electrode. Solid lines in panel d) and e) are curves resulting from the fitting procedure.

To finally elucidate the role of MXene when added to cTiO$_2$ layer, device with structure D were fabricated and compared with device type C. The electrical parameters statistics are reported in **Figure S15** while charge

extraction and TPC measurements were performed and reported in **Figure S19**. The tuning of $cTiO_2$ WF resulted in better energy level alignment at $cTiO_2$+MXene/$mTiO_2$+MXene compared to $cTiO_2$/$mTiO_2$+MXene interface by reducing the charge accumulation at such interface.

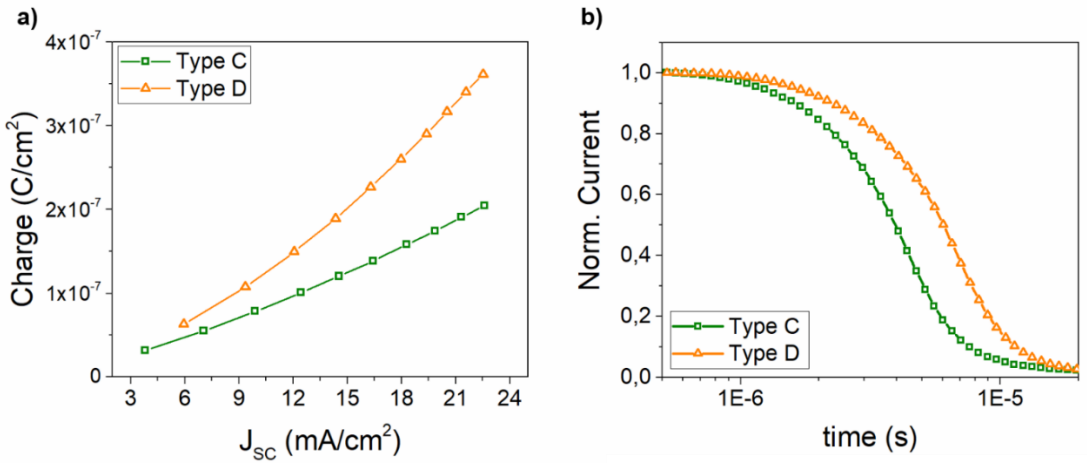

Figure S19: a) Charge density extracted and b) TPC decay profiles for devices type C and D, differing between each other only for the MXene-doped $cTiO_2$.

In order to clarify the role of MXene doping for $cTiO_2$ layer, charge extraction measurements were carried out for type C and type D PSCs differing only for the $cTiO_2$ MXene doping (**Figure S19a**).
The charge extraction experiments are performed at open circuit voltage in a small perturbation regime. When the cell is irradiated, a slight light perturbation is applied by inducing some charge. In this state, all charge carriers generated by light recombine. Then, after removing the light perturbation, immediately the solar cell is short circuited inducing a current. The charge carriers are extracted by the built-in field and lead to a current; integrating the extraction current over time yields the extracted charge. This test is repeated multiple times, each with varying light intensity. In the case of Dye Sensitized Solar Cell (DSSC) field, charge extraction technique is used to qualitatively draw the density of state distribution below the TiO_2 conduction band. Here we are not expecting any difference at $mTiO_2$ level[18] or regarding charge dynamics at $mTiO_2$/perovskite interface[19] or involving the perovskite trap-state;[20] thus any differences in term of extracted charge has to be imputed to accumulated charge at $cTiO_2$/$mTiO_2$ interface. In fact, as shown in **Figure S19a**, the charge extracted for any irradiance level (indicated with the corresponding J_{SC}) in the case of device type D is higher than charge extracted from device type C in the same irradiance condition. This can be confidently ascribed to an energy barrier created at the $cTiO_2$/$mTiO_2$+MXene interface when $cTiO_2$ is not doped with MXene, causing charge accumulation. This is also confirmed by the slowest TPC decay profile recorded in the case of structure type D, since trapped trap emission are responsible for a reduction of the current on a longer timescale (**Figure S19b**).

D) Drift-Diffusion Device Simulations

Device simulations are performed by using TIberCad multiscale simulation software (TiberLAB). The simulation tool is based on the drift-diffusion model equations,

$$\begin{cases} \nabla \cdot (\varepsilon \nabla \varphi) = -\rho \\ \nabla \cdot j_n = \nabla \cdot \left(\mu_n n \nabla \phi_n \right) = -R + G \\ \nabla \cdot j_p = \nabla \cdot \left(\mu_p p \nabla \phi_p \right) = R - G \end{cases} \quad (1)$$

where φ represents the electrostatic potential, ϕ_n and ϕ_p the electron and hole quasi Fermi potentials, while *n* and *p* the related carrier densities. In the Poisson equation, *ρ* is the total charge density, including free carrier densities, and ionized donors and acceptors. The generation (G) is modelled with a Lambert-Beer absorption. The recombination (R) includes all contributions accounted in the system, such as trap-assisted (Shockley-Read-Hall) and direct recombination model described by

$$R_{SRH} = \frac{np - n_i^2}{\tau_n \cdot \left(p + p_i \right) + \tau_p \cdot \left(n + n_i \right)} \quad (2)$$

$$R_{DIR} = k_2 \cdot \left(np - n_i^2 \right) \quad (3)$$

The parameters used for each different device are summarized in Table S1. Interface recombination at both $cTiO_2$/$mTiO_2$+perovskite and $mTiO_2$+perovskite/spiro-OMeTAD interfaces are also considered.

Layer	Parameter	Reference	Type A	Type B	Type C
TiO_2	Doping (cm^{-3})	$1x10^{20}$	$1x10^{20}$	$1x10^{20}$	$1x10^{20}$
	CB (eV)	-3.95*	-3.95*	-3.90*	-3.85*
	VB (eV)	-7.15*	-7.15*	-7.10*	-7.05*
	μ_h; μ_e ($cm^2\ V^{-1}\ s^{-1}$)	2; 0.02 [21]	2; 0.02 [21]	2; 0.02 [21]	2; 0.02 [21]
TiO_2/Perovskite	$C_{T/P}$ ($cm^4\ s^{-1}$)	$1x10^{-17}$	$3x10^{-18}$	$3x10^{-18}$	$2.5x10^{-18}$
Perovskite	Doping (cm^{-3})	$1x10^{15}$	$1x10^{15}$	$1x10^{15}$	$1x10^{15}$
	CB (eV)	-3.90	-3.55*	-3.55*	-3.55*
	VB (eV)	-5.50	-5.15*	-5.15*	-5.15*
	μ_h; μ_e ($cm^2\ V^{-1}\ s^{-1}$)	2; 2	2; 2	2; 2	4; 4
	T_{SRH} (s)	$2.25x10^{-8}$ [22]	$1.5x10^{-8}$ [22]	$1.5x10^{-8}$ [22]	$1.5x10^{-8}$ [22]
	C_{DIR} ($cm^3\ s^{-1}$)	$3x10^{-9}$ [23]	$3x10^{-9}$ [23]	$3x10^{-9}$ [23]	$3x10^{-9}$ [23]
Perovskite/Spiro	$C_{P/S}$ ($cm^4\ s^{-1}$)	$0.8x10^{-16}$	$1x10^{-16}$	$1x10^{-16}$	$1x10^{-16}$
Spiro-OMeTAD	Doping (cm^{-3})	$3x10^{16}$	$3x10^{16}$	$3x10^{16}$	$3x10^{16}$
	CB (eV)	-2.2 [24]	-2.2 [24]	-2.2 [24]	-2.2 [24]
	VB (eV)	-5.2 [24]	-5.2 [24]	-5.2 [24]	-5.2 [24]
	μ_h, μ_e ($cm^2\ V^{-1}\ s^{-1}$)	$2x10^{-3}$, $5x10^{-3}$ [25]	$2x10^{-3}$, $5x10^{-3}$ [25]	$2x10^{-3}$, $5x10^{-3}$ [25]	$2x10^{-3}$, $5x10^{-3}$ [25]
FTO	WF (eV)	-4.16*	-4.16*	-4.16*	-4.16*
Au	WF (eV)	-5.1	-5.1	-5.1	-5.1

***Table S1*: Parameters used in device simulations, where * indicates values related to UPS measurements. The rest of values are obtained from literature (reference given) or used as fitting parameters.**

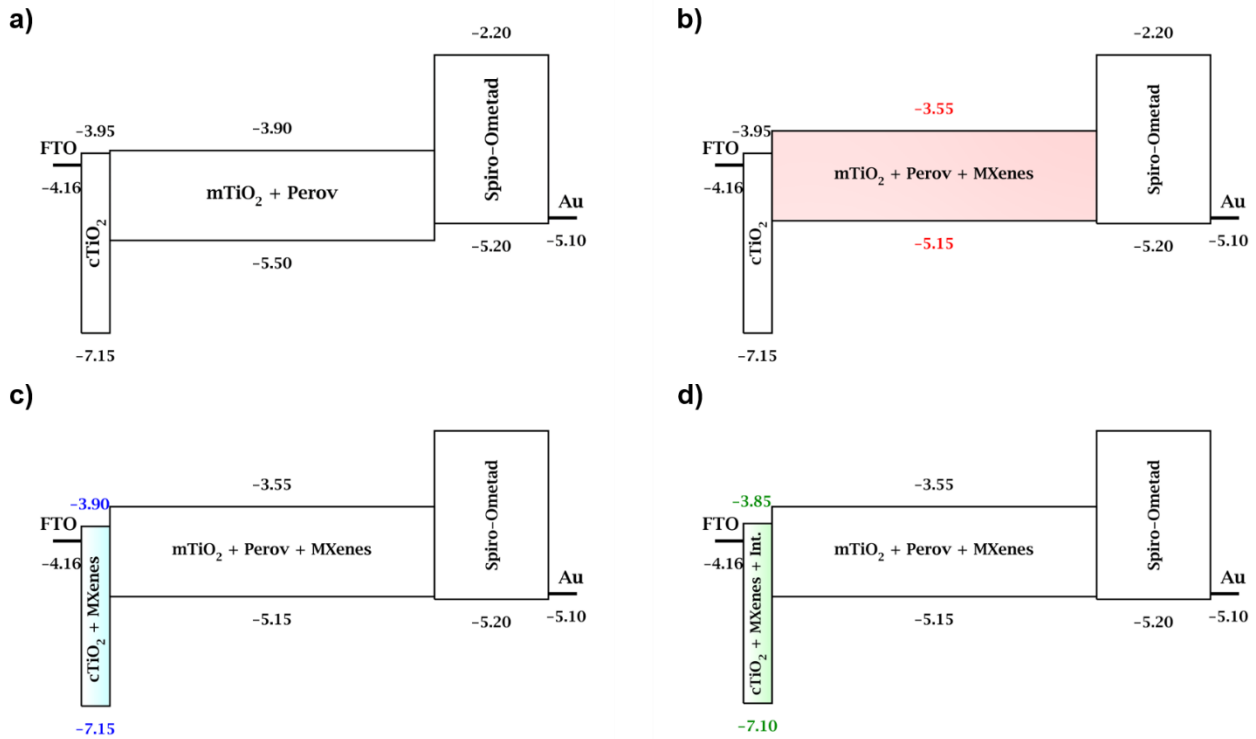

Figure S20: Schematic representation of energy band diagram for the different device structures simulated, (a) reference, (b) type A, (c) type B and (d) type C, as reported in Table S1.

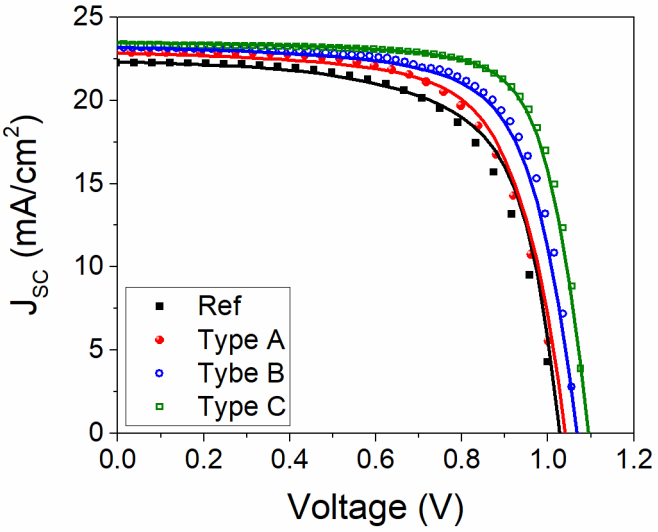

Figure S21: Comparison between theoretical (solid lines) and average experimental (dots) J-V characteristics of the different devices.

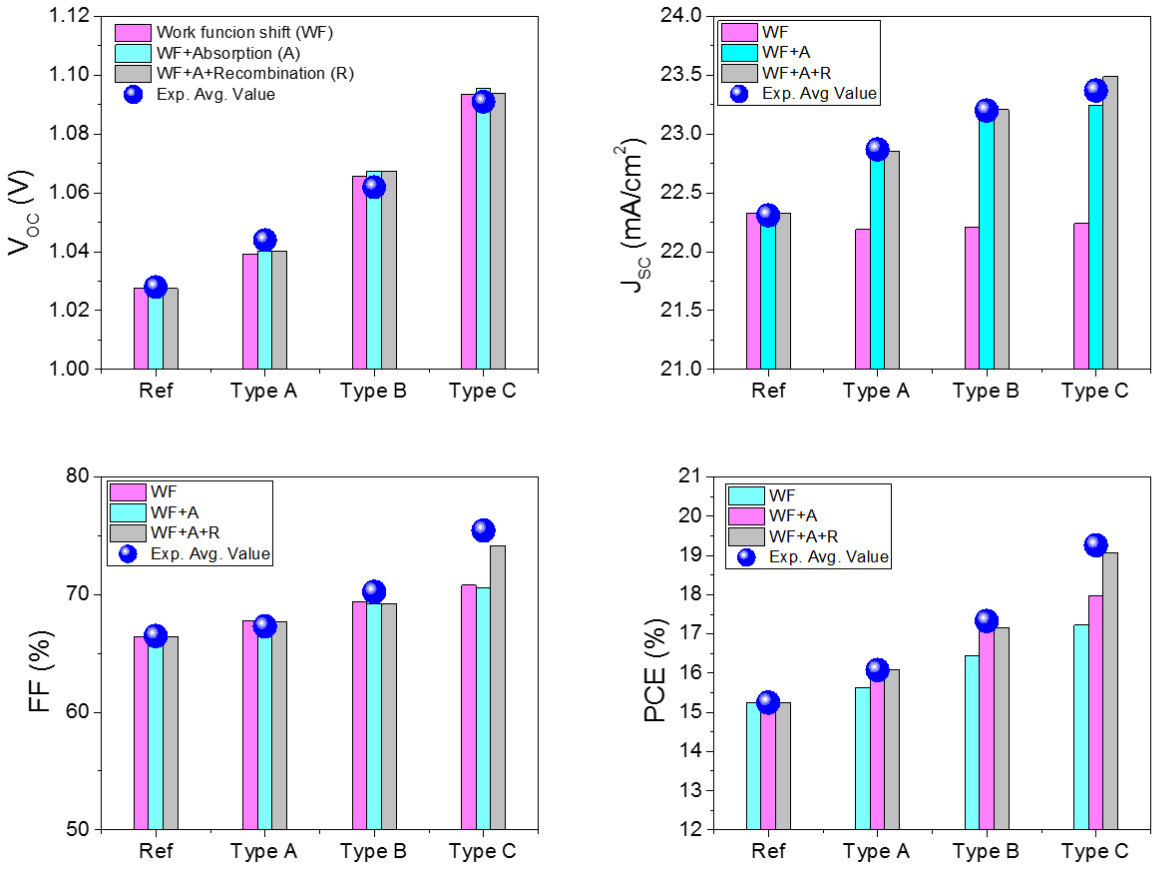

Figure S22: J-V characteristics comparison between experimental and theoretical results for all different devices modelling the inclusion of MXene as i) only work function shift (WF), ii) WF shift plus the increased light absorption of perovskite with MXene (A) and iii) WF shift, increased light absorption and adding the improved charge transfer at the perovskite/TiO_2 interface (R).

We included in the simulation an additional charge carrier generation for each device type dimensioned according to the variation of absorption spectra shown in **Figure S23a**. By integrating the normalized absorption spectrum in the range of 600-850 nm we found a percentage increase of 4% and 5% for devices comparable with type A and C, respectively. Assuming that the inclusion of MXenes within cTiO_2 could slightly reduce the effective absorption because of internal reflections, we performed the DD simulation by increasing the charge carrier generation by 3%, 4.5% and 4% for type A, B and C, respectively. This modelling allowed to reach a good match in all types concerning J_{SC}, but not for the FF in type C. This increase in FF could be explained by improved transport across the TiO_2/perovskite interface in the mesoporous layer, which has been modelled by slightly increasing the effective mobility of the perovskite as reported in **Table S1**.

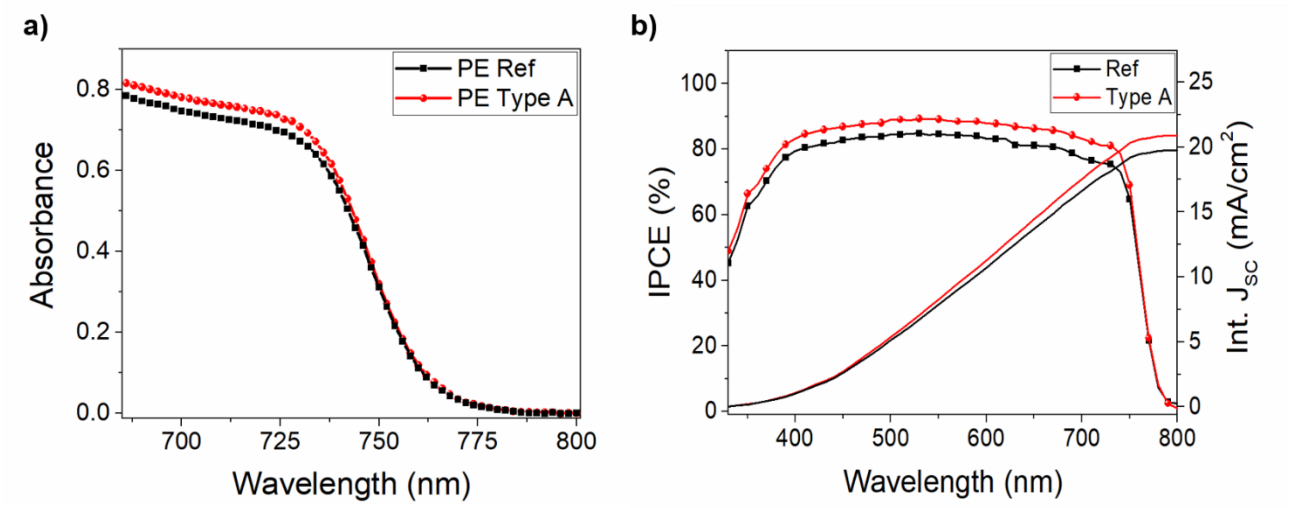

Figure S23: a) Light absorption spectra acquired on opened photo-electrodes (PE) of reference (ref) and type A devices. b) Incident photon to current conversion efficiency (IPCE) and integrated currents for reference and Type A devices

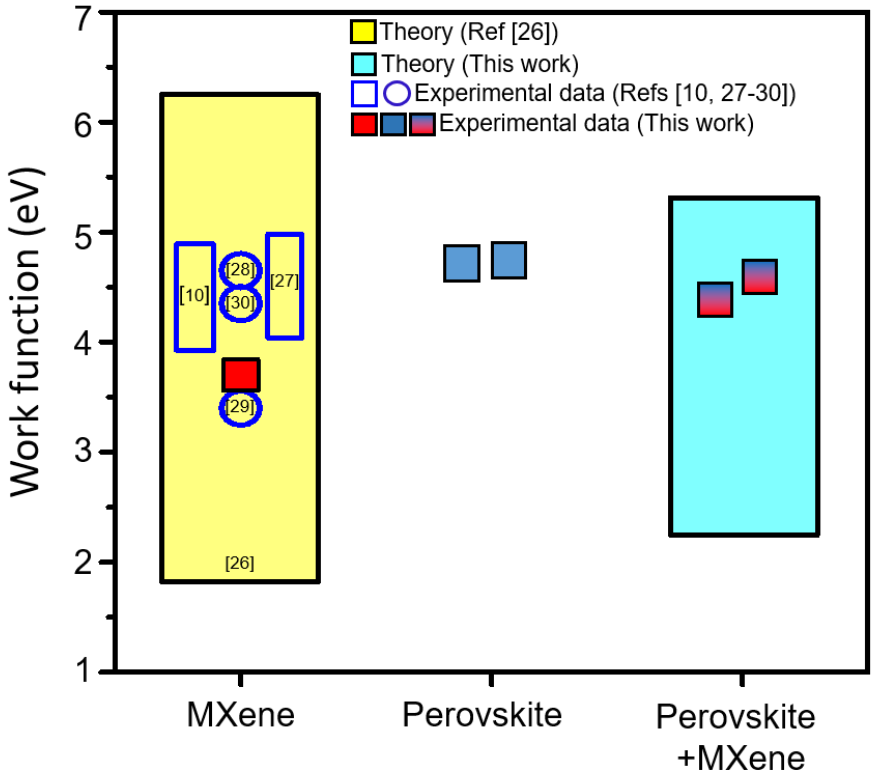

Figure S24: WF comparison between $Ti_3C_2T_x$ MXene, perovskites and MXene-doped perovskites reported in literature[10,26–30] (open symbols) and measured in the present work (full squares). The range of possible theoretical WF values of MXene as obtained in literature and the WF range for MXene-doped perovskite as calculated in the present work is also reported.

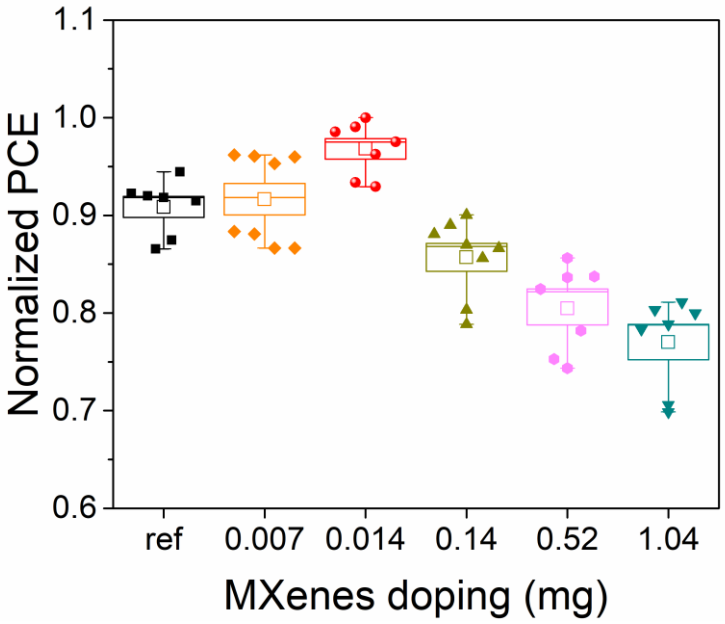

Figure S25: Normalized PCE of PSCs realized by changing the $Ti_3C_2T_x$ MXene amount used to dope 1 ml of perovskite precursor solution.

ACKNOWLEDGEMENTS

ADC and DS gratefully acknowledge the financial support from the Ministry of Education and Science of the Russian Federation in the framework of MegaGrant № 075-15-2019-872 (14.Y26.31.0027/074-02-2018-327). AA and SP gratefully acknowledge funding from the European Union's Horizon 2020 Research and Innovation Program under grant agreement no.785219-GrapheneCore2.
All the authors gratefully acknowledge Prof. E. Bemporad and Dr. D. De Felicis from LIME (Interdepartmental Electron Microscopy Lab), University of Roma Tre, for SEM characterizations.

References

1. Persson, I. *et al.* On the organization and thermal behavior of functional groups on Ti_3C_2 MXene surfaces in vacuum. *2D Mater.* **5**, 015002 (2017).
2. Persson, I. *et al.* On the organization and thermal behavior of functional groups on Ti_3C_2 MXene surfaces in vacuum. *2D Mater.* **5**, 015002 (2017).
3. Hart, J. L. *et al.* Control of MXenes' electronic properties through termination and intercalation. *Nat. Commun.* **10**, 522 (2019).
4. Giannozzi, P. *et al.* QUANTUM ESPRESSO: a modular and open-source software project for quantum simulations of materials. *J. Phys. Condens. matter* **21**, 395502 (2009).
5. Perdew, J. P. & Zunger, A. Self-interaction correction to density-functional approximations for many-electron systems. *Phys. Rev. B* **23**, 5048 (1981).
6. Perdew, J. P., Burke, K. & Ernzerhof, M. Generalized gradient approximation made simple. *Phys. Rev. Lett.* **77**, 3865 (1996).
7. Khazaei, M., Ranibar, A., Arai, M., Sasaki, T. & Yunoki, S. Electronic properties and application of

MXenes: a theoretical review. *J. Mater. Chem. C* **5**, 2488–2503 (2017).

8. Foley, B. J. *et al.* Controlling nucleation, growth, and orientation of metal halide perovskite thin films with rationally selected additives. *J. Mater. Chem. A* **5**, 113–123 (2017).

9. Liu, Y., Xiao, H. & Goddard, W. A. Schottky-Barrier-Free Contacts with Two-Dimensional Semiconductors by Surface-Engineered MXenes. *J. Am. Chem. Soc.* **138**, 15853–15856 (2016).

10. Schultz, T. *et al.* Surface termination dependent work function and electronic properties of $Ti_3C_2T_x$ MXene. *Chem. Mater.* acs.chemmater.9b00414 (2019). doi:10.1021/acs.chemmater.9b00414

11. Lotfi, R., Naguib, M., Yilmaz, D. E., Nanda, J. & Van Duin, A. C. T. A comparative study on the oxidation of two-dimensional Ti_3C_2 MXene structures in different environments. *J. Mater. Chem. A* **6**, 12733–12743 (2018).

12. McNeill, C. R., Hwang, I. & Greenham, N. C. Photocurrent transients in all-polymer solar cells: Trapping and detrapping effects. *J. Appl. Phys.* **106**, (2009).

13. Polyakov, A. Y. *et al.* Trap states in multication mesoscopic perovskite solar cells: A deep levels transient spectroscopy investigation. *Appl. Phys. Lett.* **113**, 263501 (2018).

14. Neukom, M., Züfle, S., Jenatsch, S. & Ruhstaller, B. Opto-electronic characterization of third-generation solar cells. *Sci. Technol. Adv. Mater.* **19**, 291–316 (2018).

15. Gouda, L. *et al.* Open Circuit Potential Build-Up in Perovskite Solar Cells from Dark Conditions to 1 Sun. *J. Phys. Chem. Lett.* **6**, 4640–4645 (2015).

16. Shao, S. *et al.* N-type polymers as electron extraction layers in hybrid perovskite solar cells with improved ambient stability. *J. Mater. Chem. A* **4**, 2419–2426 (2016).

17. Shao, Y., Xiao, Z., Bi, C., Yuan, Y. & Huang, J. Origin and elimination of photocurrent hysteresis by fullerene passivation in $CH_3NH_3PbI_3$planar heterojunction solar cells. *Nat. Commun.* **5**, 1–7 (2014).

18. Giordano, F. *et al.* Enhanced electronic properties in mesoporous TiO_2 via lithium doping for high-efficiency perovskite solar cells. *Nat. Commun.* **7**, 1–6 (2016).

19. Cohen, B. El, Wierzbowska, M. & Etgar, L. High efficiency quasi 2D lead bromide perovskite solar cells using various barrier molecules. *Sustain. Energy Fuels* **1**, 1935–1943 (2017).

20. Cohen, B. El, Wierzbowska, M. & Etgar, L. High Efficiency and High Open Circuit Voltage in Quasi 2D Perovskite Based Solar Cells. *Adv. Funct. Mater.* **27**, 1–7 (2017).

21. Bak, T., Nowotny, M. K., Sheppard, L. R. & Nowotny, J. Mobility of electronic charge carriers in titanium dioxide. *J. Phys. Chem. C* **112**, 12981–12987 (2008).

22. Sherkar, T. S. *et al.* Recombination in Perovskite Solar Cells: Significance of Grain Boundaries, Interface Traps, and Defect Ions. *ACS Energy Lett.* **2**, 1214–1222 (2017).

23. Wehrenfennig, C., Eperon, G. E., Johnston, M. B., Snaith, H. J. & Herz, L. M. High charge carrier mobilities and lifetimes in organolead trihalide perovskites. *Adv. Mater.* **26**, 1584–1589 (2014).

24. Chueh, C.-C., Li, C.-Z. & Jen, A. K.-Y. Recent progress and perspective in solution-processed Interfacial materials for efficient and stable polymer and organometal perovskite solar cells. *Energy Environ. Sci.* **8**, 1160–1189 (2015).

25. Hawash, Z., Ono, L. K. & Qi, Y. Recent Advances in Spiro-MeOTAD Hole Transport Material and Its Applications in Organic--Inorganic Halide Perovskite Solar Cells. *Adv. Mater. Interfaces* **5**, 1700623 (2018).

26. Khazaei, M. *et al.* OH-terminated two-dimensional transition metal carbides and nitrides as ultralow

work function materials. *Phys. Rev. B - Condens. Matter Mater. Phys.* **92**, 1–10 (2015).

27. Yu, Z. *et al.* MXenes with tunable work functions and their application as electron- and hole-transport materials in non-fullerene organic solar cells. *J. Mater. Chem. A* (2019). doi:10.1039/C9TA01195A

28. Deng, W. *et al.* All-Sprayed-Processable, Large-Area, and Flexible Perovskite/MXene-Based Photodetector Arrays for Photocommunication. *Adv. Opt. Mater.* **1801521**, 1–9 (2019).

29. Peng, C. *et al.* High efficiency photocatalytic hydrogen production over ternary Cu/TiO_2@$Ti_3C_2T_x$ enabled by low-work-function 2D titanium carbide. *Nano Energy* **53**, 97–107 (2018).

30. Kang, Z. *et al.* MXene–Silicon Van Der Waals Heterostructures for High-Speed Self-Driven Photodetectors. *Adv. Electron. Mater.* **3**, 1–7 (2017).